Journal of Materials Chemistry C

ROYAL SOCIETY OF CHEMISTRY

PAPER

View Article Online
View Journal | View Issue

Cite this: J. Mater. Chem. C, 2024, 12, 12064

Edible temperature-responsive-adhesive thermogalvanic hydrogel for self-powered multi-sited fatigue monitoring†

Xinru Zhang,[a] Ning Li,[a] Xiaojing Cui, *[bc] Yu Li,[a] Zhaosu Wang,[a] Kai Zhuo[a] and Hulin Zhang *[a]

Most traffic accidents are caused by driver fatigue, so achieving effective monitoring of fatigue status is particularly important. However, current detection methods mainly rely on complex biosensors that lack independence from power supply and adaptive adhesion, and have a risk of ingestion, especially for infants. Here, we propose an edible thermogalvanic hydrogel with I^-/I_3^- as a redox pair for self-powered physiological monitoring by coupling thermogalvanic and piezoresistive effects. The gelatin/glycerol (Gel/GL) hydrogel exhibits excellent thermo-reversible gelling and temperature-responsive adhesion that can ensure on-demand reliable adhesion to skin for capturing physiological signals under hot compress and facilitate easy removal under cold compress due to the decomplexation and re-entanglement of gelatin chains. Moreover, a low-cost passive patch based on this self-adaptable thermogalvanic gel has been invented to simultaneously monitor breathing, blinking, yawning, and pulse at the canthus, philtrum and radial artery of the human body by acquiring thermoelectric signals correlated with physiological action, achieving a self-powered accurate surveillance of fatigue status, which can provide timely reminders based on fatigue levels. This work is beneficial for improving driving safety and exhibits the potential of the designed hydrogel for application in intelligent transportation.

Received 6th April 2024,
Accepted 20th June 2024

DOI: 10.1039/d4tc01418a

rsc.li/materials-c

1. Introduction

The escalating number of vehicles on the roads contributes to a surge in frequent traffic accidents, posing a significant global challenge.[1] The vast majority of traffic accidents are caused by dangerous driving behavior, in which driver fatigue accounts for a substantial proportion.[2] Driving fatigue refers to a phenomenon where the driver has a psychological disorder and physiological functions after driving continuously for a long time, such as blurred vision, slow response and dulled movement.[3] Furthermore, the feeling of being sleepy is a gradual process and drivers are not aware of their lack of attention at this moment. Consequently, a real-time drowsiness assessment system for warning drivers when fatigue symptoms appear can avoid crashes by preventing and reducing sleep episodes, either for professionals or for particular crowds.[4]

In recent years, many driver fatigue detection methods have been proposed, such as collecting vehicle motion speed, steering wheel angle,[5,6] *etc.*, or using image processing to detect drivers' facial behaviors.[7,8] Although these methods have high accuracy, they require an external power supply and expensive equipment, which is non-portable, inconvenient and easily affected by the external environment. Researchers have proposed a self-powered driver fatigue detection method based

[a] College of Electronic Information and Optical Engineering, Taiyuan University of Technology, Taiyuan, 030024, China. E-mail: zhanghulin@tyut.edu.cn
[b] Shanxi Transportation Technology Research & Development Co., Ltd., Taiyuan 030032, China. E-mail: 20210084@sxnu.edu.cn
[c] School of Physics and Information Engineering, Shanxi Normal University, Taiyuan 030031, China

† Electronic supplementary information (ESI) available. See DOI: https://doi.org/10.1039/d4tc01418a

Xiaojing Cui

Xiaojing Cui is an associate professor at Shanxi Normal University, China. She received her PhD degree in Electronic Science and Technology from Taiyuan University of Technology in 2021. During the period of 2019 to 2020, she studied as a joint-training doctoral candidate at the Georgia Institute of Technology, USA. Her research interests include thermogalvanic devices and self-powered sensors based on diverse hydrogels.

on biological signals (such as electrocardiogram, electroencephalogram, pulse signal, *etc.*),[9–11] but it mainly relies on metal electrodes with poor stretchability (copper or aluminum) or substances harmful to the environment and human body and lacks self-adhesive properties with human skin. Therefore, it is necessary to develop a highly stretchable, self-adhesive, environmentally friendly, and low-cost monitoring route for safe driving. Hydrogels are polymer networks formed through physical or chemical cross-linking, which are favored for constructing flexible electronic devices due to their low cost, ease of processing, high flexibility, and biocompatibility.[12–15] Particularly, hydrogels can be exploited to prepare various sensors to detect strain/pressure, temperature, humidity, and gas by converting these external stimuli into measurable electrical signals.[16–18] As typical flexible thermoelectric materials, thermogalvanic hydrogels which can convert ubiquitous body heat into electricity in a continuous mode offer a wide range of potential uses, including body energy harvesting and wearable electronics.[19–22]

Herein, we report an edible and degradable gelatin electrolyte-based thermogalvanic hydrogel with I^-/I_3^- as a non-toxic redox pair for self-powered monitoring of physiological signals. The hydrogel exhibits thermoplasticity and temperature-responsive adhesion due to its primary composition of edible gelatin biopolymer and glycerol. The adhesion of the hydrogel is smartly activated upon contact with warm skin, and painless detachment is easily realized by placing an ice bag on the surface of the hydrogel. A chaotropic effect is introduced into the hydrogel, in which glycerol–water (GW) is used instead of a single water solvent, so that the thermogalvanic hydrogel has excellent frost resistance and drying resistance, and can ensure sufficient long-term thermoelectric output even in harsh environments. Meanwhile, the gelatin matrix can dissolve under mild conditions, while the iodine in the solution sublimates, thus achieving degradable and pollution-free characteristics. In addition, we have established a multi-site, high-performance, and low-cost hydrogel patch that creates a soft interface with the skin to enable dependable and long-term fatigue monitoring. Finally, the multi-factor fusion module comprehensively assesses the driver's fatigue state and alerts the driver to prevent accidents caused by drowsy driving.

2. Results and discussion

2.1 Structure and application of the Gel/GL thermogalvanic hydrogel

Although thermogalvanic ions such as $[Fe(CN)_6^{4-}]/[Fe(CN)_6^{3-}]$, $Co(II/III)(bpy)_3$, SO_4^{2-}/SO_3^{2-} and Fe^{2+}/Fe^{3+} have been reported to have decent thermopowers,[23–26] here, we selected the redox pair of I^-/I_3^- as a thermogalvanic ion couple, as it is almost non-toxic, harmless, and environmentally friendly.[27] Gelatin-based hydrogels are edible, biocompatible, and degradable because gelatin is naturally derived and endowed with thermally reversible gelling properties.[28,29] Fig. 1a illustrates the simplified operating principle of the edible Gel/GL hydrogel with the thermo-electrochemical reactions taking place at the hot and cold ends as follows:

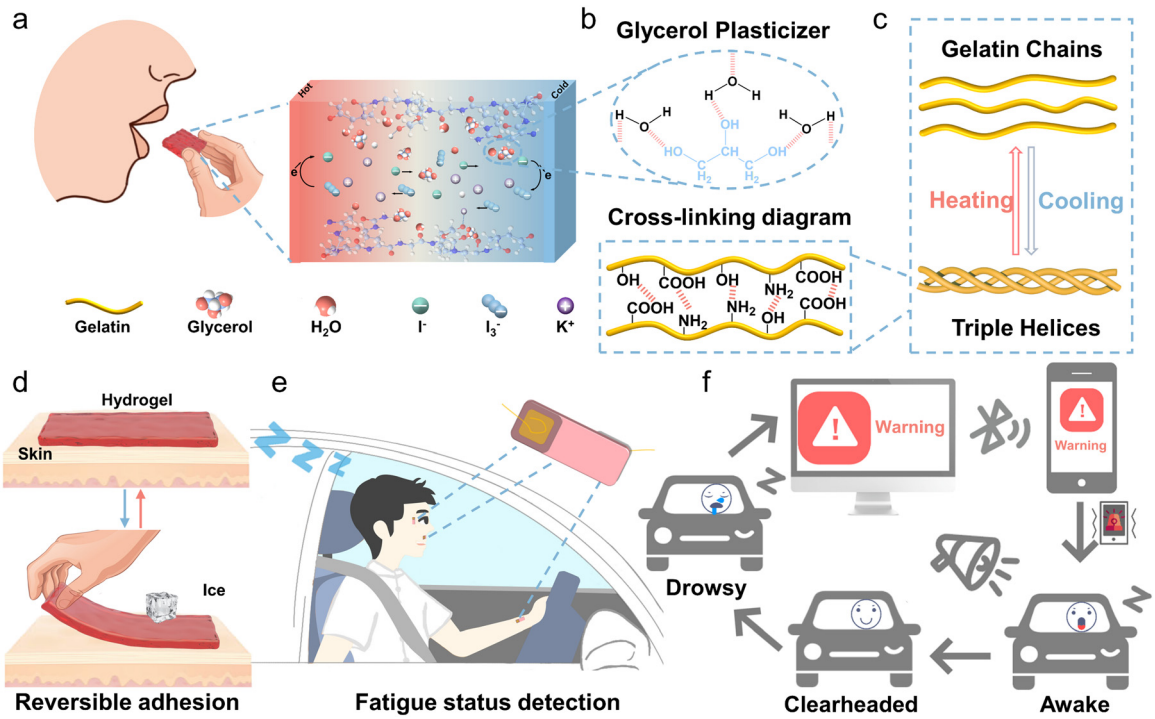

Fig. 1 Schematic structure and application of the edible Gel/GL thermogalvanic hydrogel. (a) Schematic diagram of the diffusion, redox reaction, and interaction of the ions in the Gel/GL hydrogel under the temperature gradient. (b) Effect of glycerol as a plasticizer in the hydrogel. (c) Thermo-reversible triple helix structure of gelatin. (d) Reversible adhesion of the Gel/GL hydrogel to skin. (e) Schematic diagram of fatigue status detection. (f) Schematic diagram illustrating drowsy driving behavior and the awakening process triggered by alert signals.

$$\text{Hot end: } I_3^- + 2e^- \rightarrow 3I^- \quad (1)$$

$$\text{Cold end: } 3I^- - 2e^- \rightarrow I_3^- \quad (2)$$

In addition, the interconnected porous structure exhibited in Fig. S1 (ESI†) assures favorable ion transport, enabling a continuous reaction and potential difference between the two electrodes under the temperature gradient.

To further improve the mechanical properties of gelatin and increase the solubility of electrolytes, glycerol was introduced as a plasticizer.[30] As shown in Fig. 1b, the three hydroxyl groups of glycerol form hydrogen bonds with water molecules, and the hydrogen bond of glycerol–water is more stable than that of water–water,[31] which can greatly increase the water retention capacity of the hydrogel. At the same time, these strong bonds destroy the formation of ice crystals and markedly elevate the freezing resistance. From the TG curves depicted in Fig. S2 (ESI†), it is clear that the percentage of free water in the Gel hydrogel is approximately 5.2%, while in the Gel/GL hydrogel, it dramatically decreases to 0.2%, manifesting that the addition of glycerol can significantly suppress the water loss in the Gel/GL hydrogel. From DTG plots, the degradation peaks of the composite hydrogel become less intense once glycerol is added, implying that the thermal stability of the Gel/GL hydrogel has been enhanced. Both the Gel and Gel/GL hydrogels exhibit similar main peaks, but the amplitude of the peaks varies due to the influence of glycerol. The FTIR spectra of the Gel/GL hydrogel show the presence of peaks at 1547, 1646, and 3308 cm^{-1} that correspond to amide II (N–H bending and C–H stretching), amide I (C=O stretching) and amide A (N–H stretching vibration) of gelatin, respectively (Fig. S3, ESI†). Additionally, a peak with a wavenumber of 1036 cm^{-1} is found in the Gel/GL hydrogel, corresponding to the –OH group, which primarily originates from the addition of glycerol.

This triple helix formation in gelatin is thermo-reversible (Fig. 1c) and characterized by a transition temperature. The human skin temperature can stimulate this feature, making it a temperature-controlled adhesive hydrogel without additional chemicals or equipment. Fig. 1d and Fig. S4 (ESI†) clearly depict the controllable adhesion mechanism of the Gel/GL hydrogel on the skin. Upon contact with a warm skin surface, the Gel/GL hydrogel undergoes decomplexation of gelatin chains, which is facilitated by the disruption of weak hydrogen bond interactions.[32] This process enhances the mobility of gelatin chains within the hydrogel, resulting in a soft hydrogel that readily conforms to the skin surface. Then the freely movable gelatin in the hydrogel chains will expose abundant groups, such as –OH, –COOH, and $–NH_2$, which can further form different hydrogen bonds with the skin surface and thus strengthen the interface bonding between the hydrogel and the skin.[33,34] We observed that under low-temperature conditions, the formation of stronger and more numerous intermolecular hydrogen bonds leads to the re-entanglement of gelatin chains, enhancing the cross-linking density within the Gel/GL hydrogel network. Consequently, this results in the formation of rigid hydrogels, which are difficult to make consistent contact with the skin surface.[35] Consequently, the Gel/GL hydrogel patch provides a highly gentle and minimally invasive method for skin adhesion, with the added benefit of facile removal upon cooling. Herein, we have installed the patches on a driver's face and wrist to simultaneously monitor breathing, blinking, yawning, and pulse (Fig. 1e). Once an abnormal current signal is detected, an alarm signal will be triggered and synchronously wirelessly transmitted to a cellphone for warning drivers through sound, vibration, screen images, and other means and reminding them to regain consciousness and avoid possible accidents (Fig. 1f).

2.2 Mechanical, anti-drying, anti-freezing, and self-adhesive properties of the Gel/GL hydrogel

Mechanical properties are one of the most important aspects in determining the usability of flexible hydrogels. The Gel/GL hydrogel exhibited excellent flexibility and mechanical strength, which was further evaluated under tensile and compressive conditions. As shown in Fig. 2a, the Gel/GL hydrogel shows excellent mechanical properties by tuning the glycerol volume content ($G_{vol\%}$). When the glycerol volume content increases from 0% to 50%, the tensile stress of the Gel/GL hydrogel increases from 0.075 to 0.536 MPa, and the corresponding modulus improves from 100 to 218 kPa (Fig. S5, ESI†), while the tensile strain changes from 114.5% to 364.6%. The toughness shown in Fig. S5 (ESI†), calculated from the stress–strain curves, reveals a similar positive correlation with the glycerol volume content. In particular, the toughness of the Gel/GL hydrogel with the $G_{vol\%}$ of 50 vol% reaches 941.2 kJ m^{-3}, which is approximately 18 times that of the hydrogel with the $G_{vol\%}$ of 0 vol% (52.4 kJ m^{-3}). A further increase in the $G_{vol\%}$ diminished the mechanical properties, because an excessive amount of glycerol cannot fully dissolve the gelatin monomers, thereby retarding the polymerization of polymers.[31] Hence, the Gel/GL hydrogel with the $G_{vol\%}$ of 50 vol% was employed as a representative sample for subsequent cycling tests due to its optimal mechanical properties. In addition, the I^-/I_3^- concentration might affect the mechanical properties of the hydrogel electrolyte. As the I^-/I_3^- concentration increases, the tensile stress decreases, and the corresponding modulus and toughness also decrease (Fig. S6, ESI†). The plotted loading–unloading profiles of the Gel/GL hydrogel at different strains exhibit obvious hysteresis loops, which become more and more evident with increasing strain (Fig. 2b). Besides, the fatigue resistance of the Gel/GL hydrogel was also investigated by continuous loading and unloading tests at 150% deformation, which suggests that the Gel/GL hydrogel has a rapid recovery capability and remarkable fatigue resistance (Fig. S7, ESI†). As summarized in Fig. 2c, cyclic compression–recovery processes of Gel/GL and Gel hydrogel at different degrees of specific deformations were conducted, and the illustration in the left panel shows that the initial shape can be restored after 50% compression. These results indicate that the hydrogel shows improved mechanical properties when glycerol penetrates into the gelatin network. In a nutshell, the optimized hydrogel possesses exceptional mechanical properties that precisely match those of human soft tissues (skins, muscles, *etc.*) and thus suitable for conformal wearable bioelectronics.

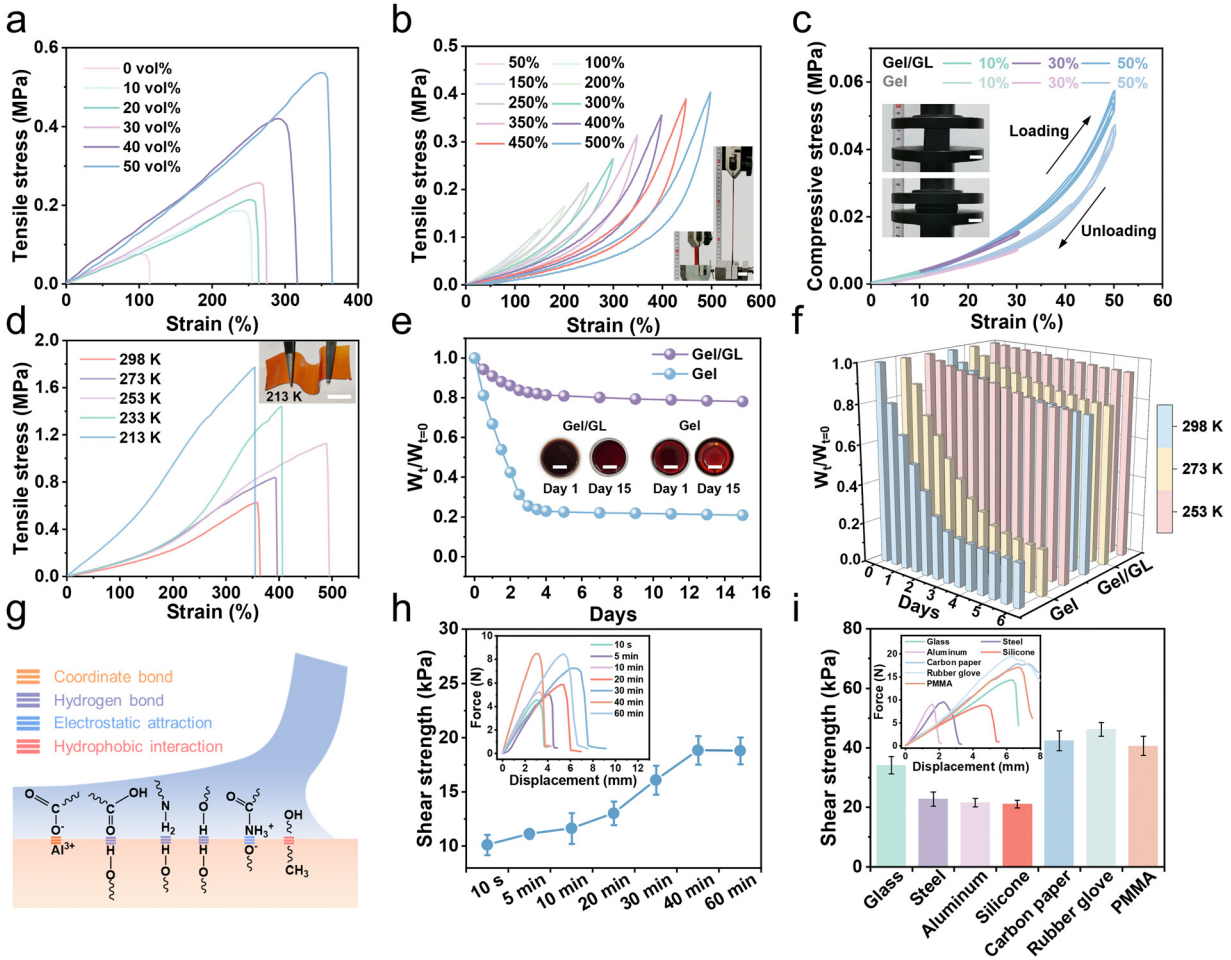

Fig. 2 Mechanical, anti-drying, anti-freezing, and self-adhesive properties of the Gel/GL hydrogel. (a) The tensile stress–strain curves of the Gel/GL hydrogel with different glycerol contents. (b) Cyclic tensile loading–unloading curves of the hydrogel with 50% glycerol under different strains. Inset: Pull-up photo of the hydrogel. (c) Cyclic compressive loading–unloading curves of Gel/GL and Gel hydrogel under different strains, the insets show a photograph of the hydrogel under compression. (d) The tensile curves of the Gel/GL hydrogel at varying temperatures. Inset: Photograph of the anti-freezing ability of the Gel/GL hydrogel. (e) Comparison of the anti-drying capacity of the Gel/GL and Gel hydrogels over 15 days at room temperature. Inset: the photo of the Gel/GL and Gel hydrogels at room temperature after 1 day and 15 days. (f) The difference in anti-drying properties of the two hydrogels at varying durations. (g) Schematic of the adhesion mechanisms. (h) Shear strength of the Gel/GL hydrogel as a function of attachment time, with insets showing the typical force–displacement curves recorded in the lap shear tests. (i) Shear strength of adhesion for different substrates (glass, steel, aluminum, silicone, carbon paper, rubber glove, and PMMA) using Gel/GL hydrogels. Scale bar: 1 cm.

In the glycerol–water binary solvent, glycerol molecules form a variety of molecular clusters with water molecules, disrupting the strong hydrogen bonds between water molecules and lowering the freezing point below 213 K. Meanwhile, without ice crystallization, the increased entropic elasticity allows the hydrogel to be mechanically adaptable in extremely cold environments. As depicted in Fig. 2d, with the decrease in temperature, the tensile properties improve, corresponding to an increase in tensile stress from 0.627 to 1.774 MPa. Based on the principle that glycerin can reduce the saturated vapor pressure of water and decrease the water loss of the hydrogel, the Gel/GL hydrogel also exhibits considerable anti-drying properties. For further analysis, the hydrogel was compared with those without GL (Gel hydrogel) at room temperature. The water loss of the hydrogels within 15 days was quantitatively evaluated using $W_t/W_{t=0}$ (anti-drying properties), where $W_{t=0}$ is the initial mass of the hydrogel and W_t is the mass at different times. As shown in Fig. 2e, the weight percentage of the hydrogel without GL is only 21% of the original weight after 15 days, while that of the Gel/GL hydrogel remains at more than 78%. Furthermore, the Gel/GL hydrogel achieves even better anti-drying properties than the Gel hydrogel in the temperature range of 253 to 298 K (Fig. 2f and Fig. S8, ESI†).

We then conducted lap shear tests on a porcine skin and engineering substrate bonded with our hydrogel for the sake of exploring the adhesion of the hydrogel to different interfaces (Fig. S9, ESI†). We attribute the strong adhesion to the presence of multiple interactions, including metal coordination, hydrogen bonds, electrostatic attraction, and hydrophobic interactions, as illustrated in Fig. 2g. In fact, the shear strength of the hydrogel is closely related to the attachment time with the human skin, which can be investigated by varying the initial

time of attachment.[36] Here, we used a wet porcine skin as the model tissue because its mechanical and biological properties are similar to those of human skin.[37] As summarized in Fig. 2h, we first allowed two pieces of porcine skin to adhere using the hydrogel for different times and measured the adhesion strength at a short timescale. Immediately after being adhered to the skin, the hydrogel displays a high shear strength of 10 kPa (within 1 min) and is sufficiently strong to prevent its delamination from the skin. As the attachment time increases, the adhesion strength increases and levels off after 40 min when the mechanical interlocking at the interface reaches equilibrium and thus achieves excellent shear strength. The hydrogel can also establish stable adhesion with other solid surfaces that are widely existing in various electronic devices (Fig. 2i and Fig. S10, ESI†). Among these substrates, the rubber glove has the highest adhesive shear strength that reaches 46.2 kPa. The superior bonding strength is mainly on account of the strong adhesive force and cohesive force of the hydrogel, which is sufficient to secure electronic devices. In addition to the strong and repeatable adhesion, it is critical to achieve easy detachment for the hydrogel. As shown in Fig. S11 (ESI†), the hydrogel adhering to the skin can be easily removed after 10 seconds of freezing without pulling the skin. The hydrogel established a soft yet nonallergic interface with the skin, which allowed nondestructive detachment and reattachment of epidermal bioelectronics on the skin for reliable and long-term health monitoring.

2.3 Thermoplasticity and degradability of the Gel/GL hydrogel

The Gel/GL hydrogel has excellent thermoplasticity, which allows it to reform easily into different shapes as required and imparts recyclability. Analogous to thermoplastics, the hydrogel is capable of being processed repeatedly which can largely reduce the economic cost and environmental burden.[38,39] In our experiment, the Gel/GL hydrogel was cut into fragments and then placed in a plastic syringe. During heating at 60 °C, the hydrogel fragments were softened and translated into a homogeneous sol state. After being injected into a desired model (car, star, "TYUT", starfish and cylinder) and stored at 4 °C for 10 min, the sol state turned into a gel state again and new desired shapes were obtained (Fig. 3a and Fig. S12 and S13, ESI†). Moreover, the remolded hydrogel is mechanically flexible to sustain deformation of stretching, demonstrating excellent re-processability and remoldability (Fig. S14, ESI†). To evaluate the reliability of the hydrogel in thermoelectricity, a series of thermoelectric comparisons was carried out. As shown in Fig. 3b, the remolded hydrogel exhibits a conductivity and Seebeck coefficient similar to the original hydrogel. Additionally, the relationship between the current and

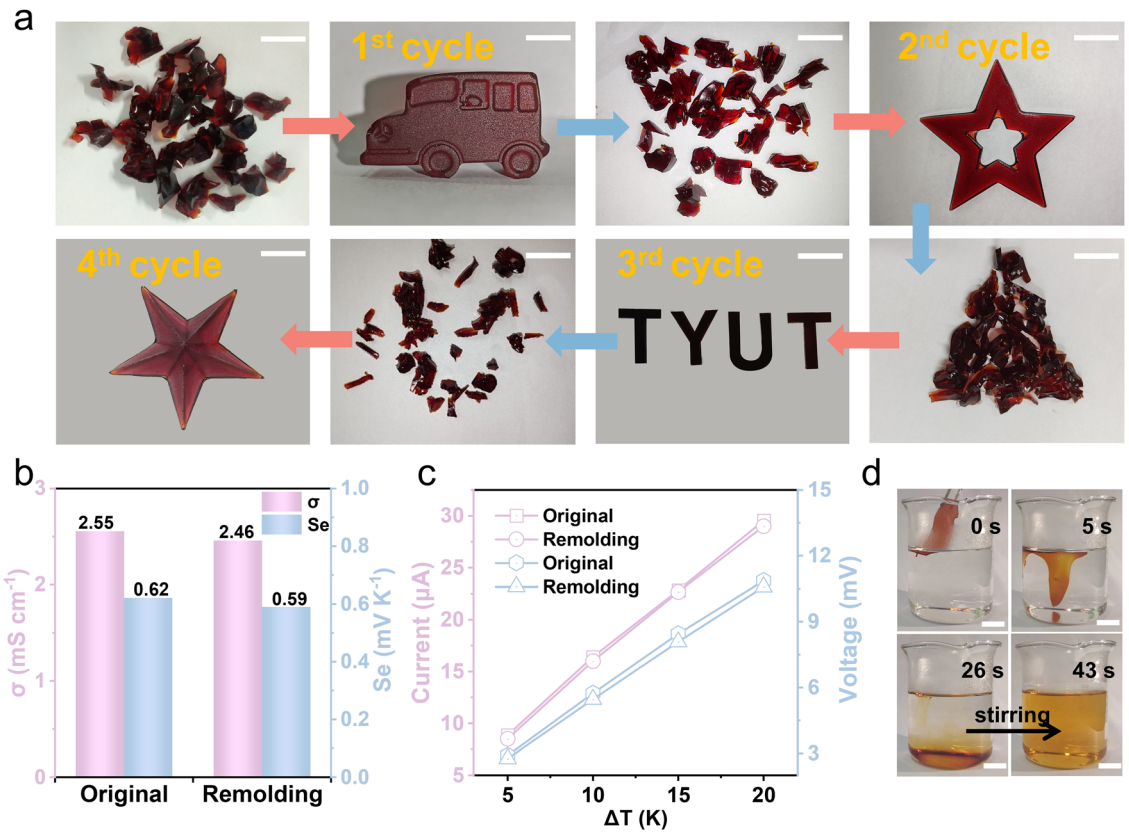

Fig. 3 Thermoplasticity and degradability of the Gel/GL hydrogel. (a) The breaking–reshaping cycle of the Gel/GL hydrogel can be repeated four times by simple heating and cooling methods. (b) Conductivity and Seebeck coefficient of the Gel/GL hydrogel before and after remodeling. (c) Current and voltage changes with temperature differences before and after the Gel/GL hydrogel remodeling. (d) Dissolution of the Gel/GL hydrogel in hot water (70 °C). Scale bar: 1 cm.

voltage of the hydrogel at different temperature differences is also investigated before and after remodeling, and there is no obvious change in the current and voltage between the reshaped and original hydrogels (Fig. 3c). Therefore, it can be concluded that the Gel/GL hydrogel is a reliable thermoplastic hydrogel that can be repeatedly processed into different shapes without changing its intrinsic thermogalvanic characteristics.

Except for the reusability, its degradability is also a significant issue worth discussing. The gelatin matrix can dissolve under mild conditions,[40] while the iodine in the solution sublimates, thus achieving degradable and pollution-free merits. To demonstrate the solubility of the Gel/GL hydrogel in water, we immersed the as-made hydrogels in water at temperatures of 40 °C, 50 °C, 60 °C, and 70 °C, respectively (Fig. S15, ESI†), showing that all hydrogels dissolve completely in water and the dissolution time declines dramatically as the water temperature increases. The hydrogel fully dissolves within 43 s at 70 °C under stirring, while the dissolution time climbs to 74 s at a temperature of 40 °C. Fig. 3d and Video S1 (ESI†) show that the softening time of the hydrogel at 70 °C is about 5 s. The hydrogel roughly dissolved in 26 s without stirring and then completely dissolved in 43 s once stirred. The solution of hydrogel dissolution becomes transparent after being stored at room temperature over 2 days (Fig. S16, ESI†), possibly due to the sublimation of iodine in the solution. The hydrogel can be degraded into harmless substances after being discarded, which contributes to environmental protection and sustainable development.

2.4 Thermoelectric properties of the Gel/GL hydrogel

The I^-/I_3^- redox couple is introduced to endow the hydrogel with the ability of heat-to-electricity conversion through the thermogalvanic effect. A hydrogel with an effective length, width, and thickness of about 20 mm, 20 mm, and 6 mm, respectively, was employed to explore thermoelectricity (Fig. S17, ESI†). The organic solvent, glycerin, significantly enhances the solubility of I_2 in water, thereby increasing the concentration of redox pairs in the hydrogel. To acquire optimal σ, hydrogels with different concentrations of I_2 and various volume ratios (r_v) of glycerol–water (GW) to gelatin were

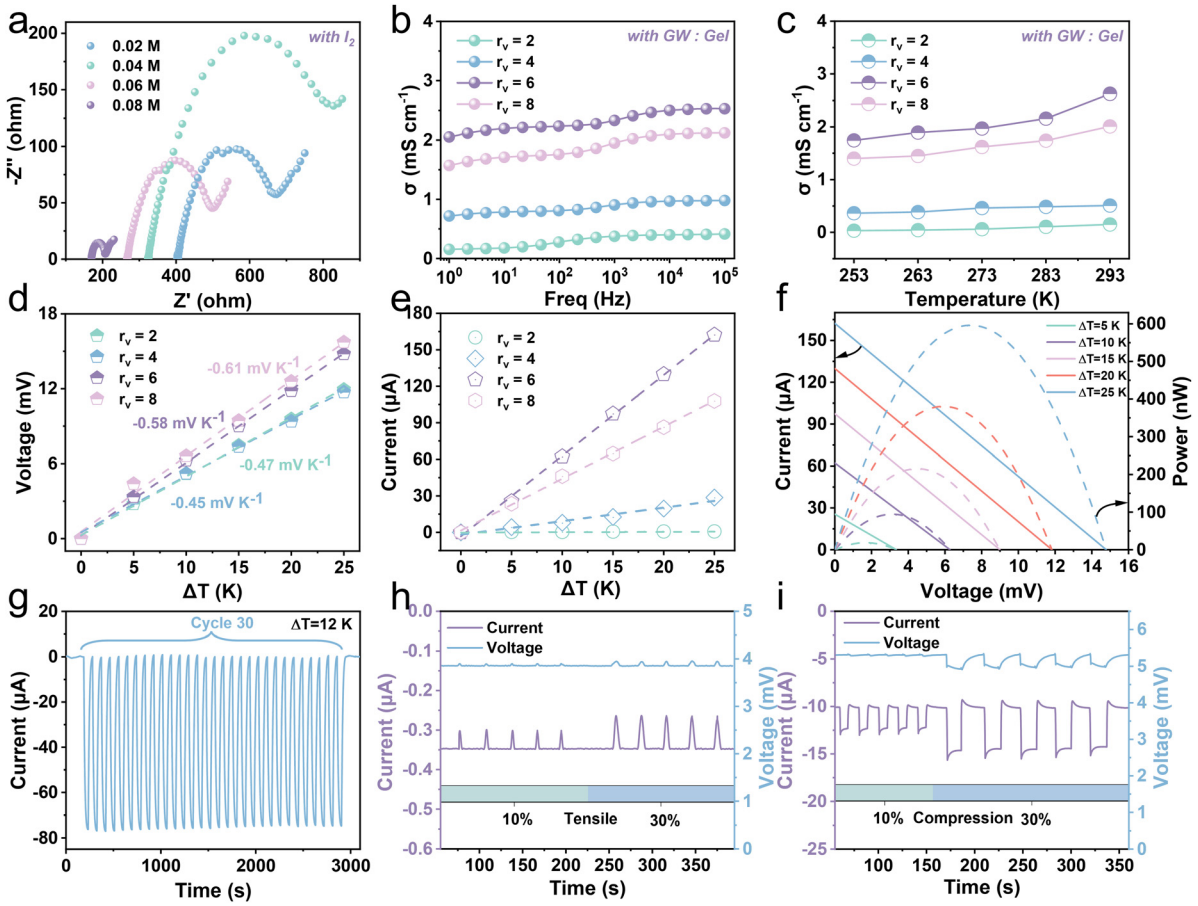

Fig. 4 Thermoelectric properties of the Gel/GL hydrogel. (a) EIS spectra with different concentrations of I_2. (b) Frequency-dependent conductance of hydrogels with different gelatin content. (c) Electrical conductivity of hydrogels with various gelatin content at different temperatures. (d) Open-circuit voltage and (e) short-circuit current of the Gel/GL hydrogel at varying ΔT. The cold terminal was fixed at 273 K. (f) Current/power–voltage curves for the Gel/GL hydrogel at varying ΔT. (g) Thirty cycles of current output at a temperature difference of 12 K. (h) Current–time (red) and voltage–time (blue) curves of Gel/GL hydrogel being repeatedly stretched when T_c = 293 K and T_h = 298 K. (i) Current–time (red) and voltage–time (blue) curves of the Gel/GL hydrogel being repeatedly pressed when T_c = 293 K and T_h = 298 K.

investigated by electrochemical impedance spectroscopy (EIS). Fig. 4a and Fig. S18 (ESI†) show the impedance change and conductivity variation of the hydrogel with the I_2 concentration. The resultant conductivity exhibits an increase with the augment of iodine monomer concentration. When the concentration of iodine monomers increases from 0.02 M to 0.08 M, the conductivity goes up from 0.21 mS cm^{-1} to 0.72 mS cm^{-1}. The r_v also affects the conductivity of the Gel/GL hydrogel (Fig. 4b). We vary the r_v value and observe a continuous increase from 0.15 to 2.05 mS cm^{-1} as r_v increases from 2 to 6. The possible reason is that as more gelatin is added, the excessive generation of bubbles in the gelatin occupies diffusion channels of ions, thereby reducing the ionic conductivity. However, further increasing r_v to 8 leads to a decrease in conductivity to 1.57 mS cm^{-1}, owing to the decline in the ion concentration. Namely, the optimal r_v is close to 6, so we fix r_v at 6 for experimental demonstration. Nevertheless, the electrical conductivity of the hydrogel increases slightly as the temperature rises, and remains in the order of 1 mS cm^{-1} (Fig. 4c and Fig. S19, ESI†). This is due to the acceleration of both the reaction rate and ion diffusion with rising temperature, leading to an increase in conductivity.

Fig. 4d shows the thermal voltage response of the hydrogel at various temperature differences (ΔT). With the increase in temperature difference, the voltage of the hydrogel with fewer gelatins is much higher than that with more gelatins with the S_e of -0.58 mV K^{-1} recorded when r_v is 6. Fig. 4e plots the current response of hydrogels with different r_v as ΔT increases, demonstrating that the current increases linearly with increasing ΔT. Among them, the current response of the hydrogel with r_v close to 6 is the most obvious. As shown in Fig. S20 (ESI†), the corresponding thermal current and voltage output of the hydrogel are stable at a constant temperature difference, and are proportional to the temperature difference provided. Through fixing the temperature of the cold end (T_c) at 273 K, the output current–voltage–power curves of the hydrogel under various ΔT are recorded (Fig. 4f). When ΔT rises from 5 to 25 K, the open-circuit voltage (V_{oc}) and short-circuit current gradually increase from 3.35 mV and 25.52 μA to 14.79 mV and 162.32 μA, respectively. The maximal power with r_v close to 6 is about 598.27 nW when the temperature difference is 25 K, while the maximum is 88.03 nW and 424.17 nW when r_v is close to 4 and 8, respectively (Fig. S21, ESI†). We also performed a cyclic test to ensure a sustainable and stable current output derived from the gel triggered by a temperature gradient. The current and voltage curves for thirty cycles at a temperature difference of 12 K are presented in Fig. 4g and Fig. S22 (ESI†). Here, the much greater temperature gradient than that between the skin and hydrogel evidently reveals outstanding stability and reliability. Furthermore, the hydrogel has exhibited good thermoelectric output capability and long-term operational stability at room temperature over a period of 15 days (Fig. S23 and S24, ESI†).

Conductive hydrogels have attracted much attention in the field of wearable sensing because of their unique piezoresistive effect.[41,42] The way of coupling thermoelectricity–piezoresistance to construct hydrogels can realize dynamic and static strain responses and obtain sensitive and reliable electrical signal output. In a room temperature environment, when a thermogalvanic gel sample is kept at the hot end of 298 K and the cold end of 293 K (ΔT = 5 K), it can produce a continuous voltage of about 3.86 mV with a stable current of about −0.35 μA. The hydrogel is stretched with strains of approximately 10% and 30% (Fig. 4h and Fig. S25, ESI†), and it is observed that the output voltage remains relatively stable while the output current exhibits distinct fluctuations. Once the force is removed, the output current quickly recovers. This evident piezoresistive effect occurs when the resistance changes after applying stimulation. Fig. S26 (ESI†) shows the current–voltage (I–V) curves of the hydrogel at different stretched strains. As the tensile strain increases, the slope of the I–V curve gradually decreases, and the resistance gradually increases, resulting in a corresponding decay in current. Furthermore, we carried out compression experiments on the hydrogel to detect the piezoresistance along the vertical direction. The output responses of the hydrogel were recorded under approximately 10% and 30% strains (Fig. 4i and Fig. S27, ESI†), and it is found that the hydrogel exhibits similar current and voltage features along both the vertical and horizontal directions. When the hydrogel is compressed and the resistance decreases, the current increases relevantly. The hydrogel can not only recover from stretching or pressing but also maintain an almost constant voltage, and the correlated current varies with the strain-stimulated resistance change. Furthermore, we compared the Gel/GL hydrogel with existing thermogalvanic gel in terms of the comprehensive performances (Fig. S28, ESI†). It is clearly observed that our proposed Gel/GL hydrogel has exceptional performance.

2.5 Driver multidimensional information monitoring system

By coupling thermogalvanic and piezoresistive effects, the proposed hydrogel is applied to monitor drivers' fatigue and physical abnormalities in a self-powered way. Under fatigue, a person's breathing and pulse become different from the normal, that is, the breathing rate decreases with the pulse quickening conversely. Concurrently, drivers exhibiting signs of drowsiness often encounter issues with ocular control, physiologically manifesting as rapid blinking at the onset of somnolence and slow blinking as fatigue intensifies. Moreover, yawning is a prominent feature of fatigue, which can also be reflected in fatigue signals. As shown in Fig. 5a, a schematic diagram of fatigue monitoring is sketched. The hydrogels are attached to the canthus, philtrum, and radial artery, respectively, to recognize fatigue behaviors (Fig. S29, ESI†). When drivers are fatigued while driving, their body temperatures rise due to dysfunction caused by excessive fatigue. The thermoelectric signals will vary correlatively, responding to small disturbances in the face areas by coupling thermogalvanic and piezoresistive effects. Therefore, the driver's physical information, including breathing, blinking, yawning, and pulse rate, can be accurately collected, and the fatigue and physical abnormalities can be determined by analyzing the current signals.

As depicted in Fig. 5b, the schematic diagram illustrates the disturbances of a hydrogel patch during breathing that is

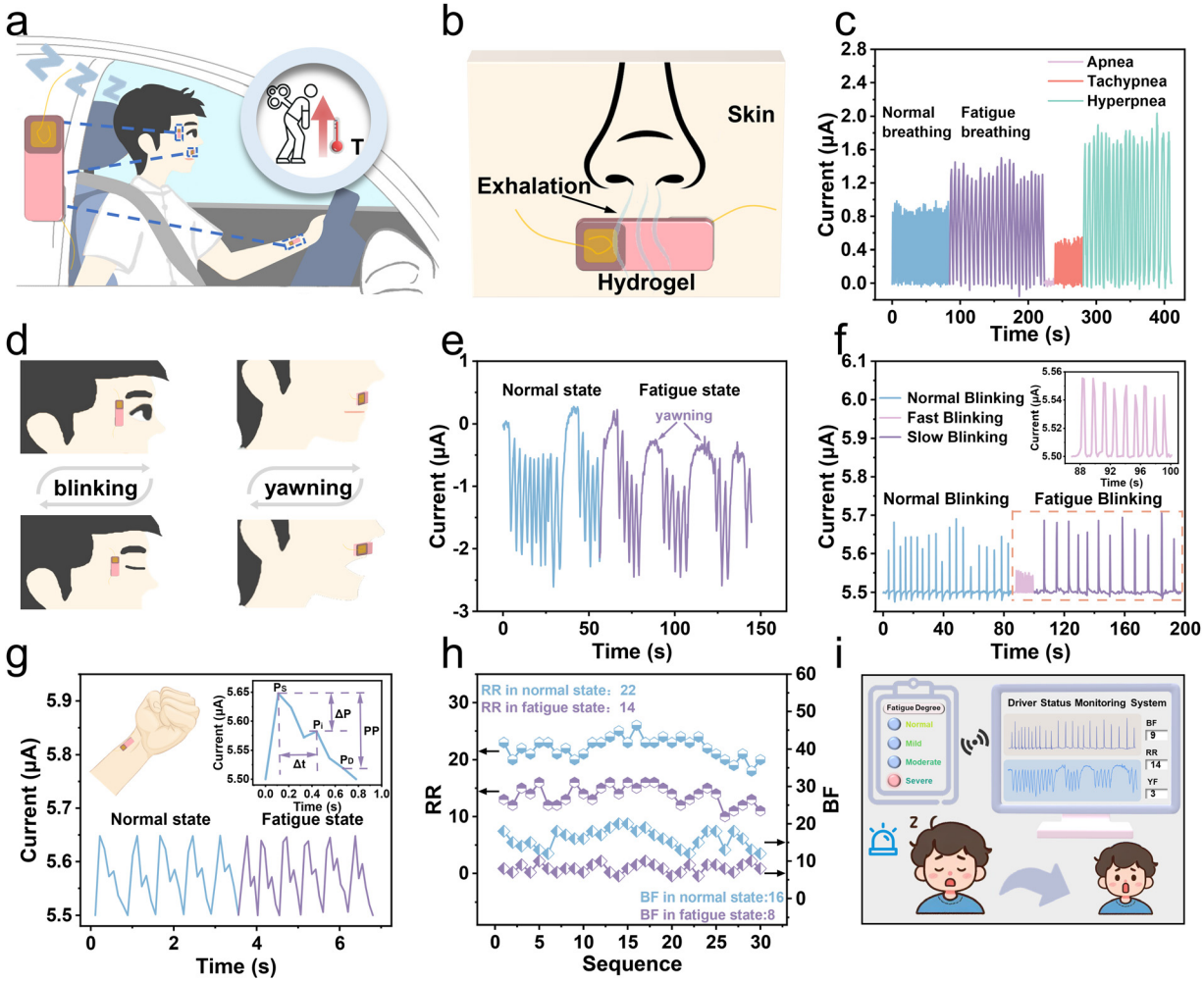

Fig. 5 Driver multidimensional information monitoring system based on the Gel/GL hydrogel. (a) Schematic illustration of the position of the hydrogel patches on the body. (b) Schematic diagram of breathing measurements. (c) Frequency and intensity changes of respiratory signals monitored under different states. (d) Schematic diagram of blinking and yawning. (e) Yawning waveform under normal and fatigue driving states. (f) Blink frequency signals detected from the canthus. The illustration shows an enlarged blink waveform. (g) Normal and fatigue pulse waves detected by the hydrogel patch. The illustration shows the schematic diagram of pulse monitoring and the characteristic peaks of pulse waves. (h) RR and BF under normal and fatigue driving states. (i) Schematic diagram of the monitoring system interface.

attached to the philtrum to grab breathing signals in real-time based on the temperature difference between the exhalation and the human skin surface. Fig. S30 (ESI†) shows the temperature distribution during respiration on the hydrogel. We used the hydrogel patch to successfully acquire the current signals during normal and fatigue breathing (Fig. 5c). When exhaling, as the temperature difference increases, the current increases accordingly, and conversely, during inhalation, the current returns to its initial value (Fig. S31, ESI†). When a person feels tired after driving for a long time, he will exhibit a slower breathing rate. Additionally, three abnormal breathing patterns (apnea, tachypnea, and hyperpnea) can be clearly and accurately detected to prevent sudden illnesses while driving. The small disturbances of a hydrogel patch on a canthus or philtrum during blinking or yawning are sketched in Fig. 5d. Fig. 5e shows the current waveform during an entire yawning process that can accurately monitor the driver's fatigue by analyzing yawning behaviors. Furthermore, the patch on the canthus can produce discriminable current waveforms triggered by opening and closing of the eyes (Fig. 5f). Due to the temperature difference between the skin and the room temperature environment, in the initial open-eye state, the current has an original value of 5.5 μA. Upon closure, the patch perceptively identifies the subtlety of ocular motility as a result of an increasing current. Once the eye is open again, the current will decrease and return to its initial value. Drivers in a state of mild fatigue tend to resist fatigue by blinking frequently, resulting in a higher blinking frequency than normal. In contrast, under severe fatigue, their eyes become dull, and the blinking frequency dramatically decreases accordingly. Therefore, if the flashing frequency is too slow or too fast, it indicates that the driver is in a state of fatigue. As shown in Fig. 5g, the real-time pulse wave signal can be efficiently recorded by attaching a hydrogel patch to the radial artery.

When a person is under fatigue, the pulse beats faster. What's more, the gel can clearly detect the characteristic peaks of pulse waves, providing the basis for accurate extraction of physiological parameters related to cardiovascular health. More specifically, there are three critical feature points of pulse waves, including the peak of the advancing wave (P_s), the peak of the reflected wave (P_i), and the peak of the dicrotic wave (P_d). These peaks can be employed to further calculate the detailed feature parameters for artery evaluation.

To assess fatigue more accurately, we divided the fatigue into four levels, including normal driving, mild, moderate, and severe fatigue, which is determined by three parameters (respiratory rate (RR), blink frequency (BF), and yawn frequency (YF)). The specific judgment flowchart of driver fatigue is depicted in Fig. S32 (ESI†). The judgment condition of severe fatigue is that all three parameters exceed the corresponding thresholds. Moderate fatigue is defined as exceeding two of the three parameters. Only one parameter exceeding the threshold indicates mild fatigue, and all parameters inferior to the thresholds indicate unfatigued. The threshold value (RR: 17 and BF: 11) is taken as the average of the highest and lowest values in fatigue and normal. Based on the actual situation and referring to the threshold setting in the literature report, we set the threshold of YF to 2.[2] The captured signals were analyzed to extract parameters and set reasonable thresholds, enabling the assessment of the driver's fatigue level. Six volunteers were invited, whose specific information is shown in Table S1 (ESI†). Because the human body is relatively awake and tired at 9 a.m. and 2 p.m., we collected 5 sets of 1 min signals in both normal and fatigue states, resulting in 60 sets of 1 min current waveforms (normal state: 30 sets, fatigued state: 30 sets) (Table S2, ESI†). The RR and BF values in normal and fatigue states are plotted in Fig. 5h, indicating that both the RR and BF values during fatigue are lower than those in the normal state, possibly due to slow breathing and blinking of the driver when fatigued, leading to a decrease in output current frequency. The monitoring interface depicted in Fig. 5i presents the detection outcomes, which encompass the output current waveforms, parameter values, and the degree of the driver's fatigue. The signal is directly synchronized and transmitted to the smartphone through a wireless communication module, which then conveys alert signals to the driver *via* sound and screen image, prompting the driver to regain awareness (Video S2, ESI†). In short, the biological information is converted actively into electrical signals by the hydrogel and then transmitted to smart terminals for further analysis. Based on the predetermined thresholds, we can realize a self-powered assessment of the fatigue level, and promptly alert the driver to prevent potentially dangerous accidents.

3. Conclusions

In conclusion, we have successfully prepared edible gelatin-based thermogalvanic hydrogels with non-toxic I^-/I_3^- as redox pairs, enabling self-powered real-time status monitoring. The glycerol plasticizer introduced to improve the mechanical properties greatly increases the frost resistance of the hydrogel, inhibits water loss, and provides the hydrogel with excellent drying resistance. The hydrogel has thermal reversibility, which can achieve non-destructive adhesion and painless skin separation in response to temperature changes. In addition, the Gel/GL hydrogel can be degraded into harmless substances after being discarded, contributing to environmental protection and sustainable development. By pasting the hydrogel on the skin, we have constructed a driver multidimensional information monitoring system based on the Gel/GL hydrogel, which can provide detailed information on driver fatigue and physical abnormalities by real-time monitoring of the driver's vital signs, such as breathing, blinking, yawning, and pulse. This work is of great significance for the further development of driver condition monitoring and also shows the great potential of Gel/GL hydrogel in the field of intelligent transportation.

4. Experimental section

4.1 Materials

KI (MW = 166, ≥99%), I_2 (MW = 253.81, ≥99.8%), glycerol (MW = 92.09, ≥99%), and gelatin (photographic grade) were purchased from Aladdin Industrial Corporation. Deionized water was purified using a Milli-Q Direct 8 ultrapure water system (Millipore, Billerica, MA). All chemicals were used without further purification.

4.2 Preparation of the Gel/GL hydrogel

Firstly, 10 ml of distilled water was mixed with 10 ml of glycerol, and then the mixture was divided into two parts. I_2 (0.406 g) and KI (0.812 g) were added to a mixture of 5 ml of water and glycerol, and magnetically stirred at 80 °C for 30 minutes to generate solution 1. Gelatin (3.77 g) particles were dissolved into the remaining mixture at 60 °C and stirred for 30 minutes to produce solution 2. The cooled solution 1 was mixed with solution 2 and stirred magnetically at 60 °C for 2 h to obtain a uniform and viscous solution. After defoaming, the Gel/GL solution was poured into the mold, frozen at −20 °C for 24 h, and then thawed at room temperature for 1 h to prepare the hydrogel.

4.3 Characterization

SEM (Hitachi SU8010) was utilized to characterize the morphology of the Gel/GL hydrogel. The mechanical properties of the hydrogel were measured using a universal mechanical test machine (QT-1196). The tensile test was conducted on rectangular samples (25 mm × 5 mm × 3 mm) at 100 mm min^{-1}. The compressive test was conducted on cube samples (20 mm × 20 mm × 20 mm) at 5 mm min^{-1}. The thermovoltage and current were measured using a Keithley 2400 instrument. The temperature of two Peltier chips was controlled by a direct current source and recorded by thermocouples (NAPUI TR230X). At the hot end of 298 K and the cold end of 293 K (ΔT = 5 K), measurements of thermoelectric current and voltage changes were taken when the tensile

specimen (25 mm × 5 mm × 3 mm) and the thermoelectric test sample (20 mm × 20 mm × 6 mm) were subjected to approximately 10% and 30% tensile stress and pressure, respectively. An electrochemical workstation (CHI660E, Shanghai Chenhua Instrument Co. Ltd) was utilized to perform electrochemical AC impedance spectroscopy of the gels, which was further used to characterize the resistance of the hydrogel. The ionic conductivity can be calculated by $\sigma = L/(A \times R)$, where σ is the ionic conductivity, L is the thickness of the gel, R is the volume resistance, and A is the contact area between the gel and the electrodes. A thermogravimetric analyzer (TGA-601, HUIC) was used to conduct thermogravimetric analysis under an air atmosphere with a scan rate of 20 °C min^{-1}.

All experiments were performed in compliance with the relevant guidelines. All human subjects provided written informed consent.

Data availability

The data supporting this article have been included as part of the ESI.†

Conflicts of interest

There are no conflicts to declare.

Acknowledgements

This work is supported by the Shanxi Province Science Foundation (20210302123190) and the Special Project of Science and Technology Cooperation and Exchange of Shanxi Province (202304041101021).

References

1 H. E. Rosen, I. Bari, N. Paichadze, M. Peden, M. Khayesi, J. Monclús and A. A. Hyder, *Injury*, 2022, S0020138322005046.
2 F. Luo, B. Chen, X. Ran, W. Ouyang and L. Shang, *Chem. Eng. J.*, 2023, **451**, 138961.
3 H. Jia, Z. Xiao and P. Ji, *Comput. Graph.*, 2022, **108**, 22–33.
4 F. Guede-Fernandez, M. Fernandez-Chimeno, J. Ramos-Castro and M. A. Garcia-Gonzalez, *IEEE Access*, 2019, **7**, 81826–81838.
5 Z. Xie, Z. Zeng, Y. Wang, W. Yang, Y. Xu, X. Lu, T. Cheng, H. Zhao and Z. L. Wang, *Nano Energy*, 2020, **68**, 104360.
6 Y. Xu, W. Yang, X. Yu, H. Li, T. Cheng, X. Lu and Z. L. Wang, *ACS Nano*, 2021, **15**, 7271–7278.
7 B. Akrout and W. Mahdi, *J. Ambient. Intell. Humaniz. Comput.*, 2023, **14**, 527–552.
8 F. You, Y. Li, L. Huang, K. Chen, R. Zhang and J. Xu, *Multimed. Tools Appl.*, 2017, **76**, 14869–14886.
9 W. Song, B. Gan, T. Jiang, Y. Zhang, A. Yu, H. Yuan, N. Chen, C. Sun and Z. L. Wang, *ACS Nano*, 2016, **10**, 8097–8103.
10 X. Ran, F. Luo, Z. Lin, Z. Zhu, C. Liu and B. Chen, *Nano Res.*, 2022, **15**, 5500–5509.
11 Y. Su, G. Chen, C. Chen, Q. Gong, G. Xie, M. Yao, H. Tai, Y. Jiang and J. Chen, *Adv. Mater.*, 2021, **33**, 2101262.
12 N. Tang, Z. Peng, R. Guo, M. An, X. Chen, X. Li, N. Yang and J. Zang, *Polymers*, 2017, **9**, 688.
13 Z. Wang, H. Li, Z. Tang, Z. Liu, Z. Ruan, L. Ma, Q. Yang, D. Wang and C. Zhi, *Adv. Funct. Mater.*, 2018, **28**, 1804560.
14 Y. Fang, G. Li, C. Huang, K. Huang, Y. Zhao, T. Nie and J. Wu, *Int. J. Biol. Macromol.*, 2023, **229**, 123–135.
15 Z. Wu, P. Zhang, H. Zhang, X. Li, Y. He, P. Qin and C. Yang, *J. Hazard. Mater.*, 2022, **421**, 126754.
16 J. Wu, Z. Wu, S. Han, B.-R. Yang, X. Gui, K. Tao, C. Liu, J. Miao and L. K. Norford, *ACS Appl. Mater. Interfaces*, 2019, **11**, 2364–2373.
17 G. Ge, Y. Lu, X. Qu, W. Zhao, Y. Ren, W. Wang, Q. Wang, W. Huang and X. Dong, *ACS Nano*, 2020, **14**, 218–228.
18 Z. Deng, T. Hu, Q. Lei, J. He, P. X. Ma and B. Guo, *ACS Appl. Mater. Interfaces*, 2019, **11**, 6796–6808.
19 C.-G. Han, X. Qian, Q. Li, B. Deng, Y. Zhu, Z. Han, W. Zhang, W. Wang, S.-P. Feng, G. Chen and W. Liu, *Science*, 2020, **368**, 1091–1098.
20 P. Yang, K. Liu, Q. Chen, X. Mo, Y. Zhou, S. Li, G. Feng and J. Zhou, *Angew. Chem., Int. Ed.*, 2016, **55**, 12050–12053.
21 Y. Zhang, J. Wang, P. Wang, X. Fan, X. Li, J. Fu, S. Li, H. Fan and Z. Guo, *J. Biomed. Mater. Res.*, 2013, **101B**, 584–590.
22 H. Ding, Z. Wu, H. Wang, Z. Zhou, Y. Wei, K. Tao, X. Xie and J. Wu, *Mater. Horiz.*, 2022, **9**, 1935–1946.
23 Z. He and W. Yuan, *ACS Appl. Mater. Interfaces*, 2021, **13**, 1474–1485.
24 C. Bai, Z. Wang, S. Yang, X. Cui, X. Li, Y. Yin, M. Zhang, T. Wang, S. Sang, W. Zhang and H. Zhang, *ACS Appl. Mater. Interfaces*, 2021, **13**, 37316–37322.
25 G. Chen, W. Xu and D. Zhu, *J. Mater. Chem. C*, 2017, **5**, 4350–4360.
26 X. Chen, J. Zhou, J. B. Goodenough and L. Shi, *J. Mater. Chem. C*, 2015, **3**, 10500–10508.
27 H. Wang, W. Xie, B. Yu, B. Qi, R. Liu, X. Zhuang, S. Liu, P. Liu, J. Duan and J. Zhou, *Adv. Energy Mater.*, 2021, **11**, 2100481.
28 M. Stevenson, J. Long, P. Guerrero, K. D. L. Caba, A. Seyfoddin and A. Etxabide, *Food Hydrocolloids*, 2019, **96**, 65–71.
29 A. N. Sardesai, X. M. Segel, M. N. Baumholtz, Y. Chen, R. Sun, B. W. Schork, R. Buonocore, K. O. Wagner and H. M. Golecki, *MRS Adv.*, 2018, **3**, 3003–3009.
30 D. Hardman, T. George Thuruthel and F. Iida, *NPG Asia Mater.*, 2022, **14**, 11.
31 L. Han, K. Liu, M. Wang, K. Wang, L. Fang, H. Chen, J. Zhou and X. Lu, *Adv. Funct. Mater.*, 2018, **28**, 1704195.
32 I. Steyaert, H. Rahier, S. Van Vlierberghe, J. Olijve and K. De Clerck, *Food Hydrocolloids*, 2016, **57**, 200–208.
33 W. Liu, R. Xie, J. Zhu, J. Wu, J. Hui, X. Zheng, F. Huo and D. Fan, *npj Flexible Electron.*, 2022, **6**, 68.
34 L. Zhou, C. Dai, L. Fan, Y. Jiang, C. Liu, Z. Zhou, P. Guan, Y. Tian, J. Xing, X. Li, Y. Luo, P. Yu, C. Ning and G. Tan, *Adv. Funct. Mater.*, 2021, **31**, 2007457.
35 Y. Jiang, X. Zhang, W. Zhang, M. Wang, L. Yan, K. Wang, L. Han and X. Lu, *ACS Nano*, 2022, **16**, 8662–8676.
36 C. Shao, L. Meng, C. Cui and J. Yang, *J. Mater. Chem. C*, 2019, **7**, 15208–15218.

37 J. Li, A. D. Celiz, J. Yang, Q. Yang, I. Wamala, W. Whyte, B. R. Seo, N. V. Vasilyev, J. J. Vlassak, Z. Suo and D. J. Mooney, *Science*, 2017, **357**, 378–381.
38 Z. Qin, D. Dong, M. Yao, Q. Yu, X. Sun, Q. Guo, H. Zhang, F. Yao and J. Li, *ACS Appl. Mater. Interfaces*, 2019, **11**, 21184–21193.
39 X. Zhang, X. Yang, Q. Dai, Y. Zhang, H. Pan, C. Yu, Q. Feng, S. Zhu, H. Dong and X. Cao, *J. Mater. Chem. B*, 2021, **9**, 176–186.
40 H. Song, H. Wang, T. Gan, S. Shi, X. Zhou, Y. Zhang and S. Handschuh-Wang, *Adv. Mater. Technol.*, 2023 2301483.
41 Z. Hu, J. Li, X. Wei, C. Wang, Y. Cao, Z. Gao, J. Han and Y. Li, *ACS Appl. Mater. Interfaces*, 2022, **14**, 45853–45868.
42 Y. Wan, Y. Wang and C. F. Guo, *Mater. Today Phys.*, 2017, **1**, 61–73.